Chinese Chemical Letters 36 (2025) 110260

Contents lists available at ScienceDirect

Chinese Chemical Letters

journal homepage: www.elsevier.com/locate/cclet

Tuning TM–O interaction by acid etching in perovskite catalysts boosting catalytic performance

Yanyu Jin[a,b], Wenzhe Si[b], Xing Yuan[b], Hongjun Cheng[b], Bin Zhou[b], Li Cai[b], Yu Wang[c], Qibao Wang[a,*], Junhua Li[b]

[a] School of Chemical and Environmental Engineering, China University of Mining &Technology (Beijing), Beijing 100083, China
[b] State Key Joint Laboratory of Environment Simulation and Pollution Control, School of Environment, Tsinghua University, Beijing 100084, China
[c] Yancheng Institute of Technology, Yancheng 224007, China

ARTICLE INFO

Article history:
Received 18 January 2024
Revised 12 July 2024
Accepted 15 July 2024
Available online 16 July 2024

Keywords:
Acid etching
TM-O interaction
Oxygen vacancy
$LaFeO_3$ perovskites
Heterogeneous
Catalytic oxidation

ABSTRACT

Perovskite oxides have been widely applied as an effective catalyst in heterogeneous catalysis. However, the rational design of active catalysts has been restricted by the lack of understanding of the electronic structure. The correlations between surface properties and bulk electronic structure have been ignored. Herein, a simple handler of $LaFeO_3$ with diluted HNO_3 was employed to tune the electronic structure and catalytic properties. Experimental analysis and theoretical calculations elucidate that acid etching could raise the Fe valence and enhance Fe–O covalency in the octahedral structure, thereby lessening charge transfer energy. Enhanced Fe–O covalency could lower oxygen vacancy formation energy and enhance oxygen mobility. *In-situ* DRIFTS results indicated the inherent adsorption capability of Toluene and CO molecules has been greatly improved owing to higher Fe–O covalency. As compared, the catalysts after acid etching exhibited higher catalytic activity, and the T_{90} had a great reduction of 45 and 58 °C for toluene and CO oxidation, respectively. A deeper understanding of electronic structure in perovskite oxides may inspire the design of high-performance catalysts.

In the critical period of environmental remediation, volatile organic compounds (VOCs) emissions and CO, derived from petroleum refining, synthetic resin manufacture, and coating, *etc.*, have aroused considerable concern due to the potential hazards to the environment and human health [1–3]. Catalytic oxidation is an effective and cost-effective way to alleviate VOCs and CO environmental pollution [4,5]. Howbeit, the booming cost and poisoning risk of precious metal catalysts have inhibited the widespread application of the technologies in the cost-conscious manufacturing enterprise. It is an urgent and obligatory business to seek alternative materials. Perovskite-type catalysts came onto our horizon owing to numerous excellent peculiarities, such as manufacturable rich defects, excellent structural flexibility, unique electronic state, and tunable metal-oxygen bonding [6,7]. Nevertheless, the ideal perovskites have an inherent deficiency, namely surface inactive A-site cation [8]. This inevitably limits the expression of high catalytic activity. One straightforward strategy to further improve the catalytic properties for perovskite-based catalysts is surface etching.

It is widely known that acid etching could produce a small concentration of A-site deficiency and create oxygen vacancies, which is conducive to catalytic oxidation of CO and VOCs [9,10]. The possibility of selective dissolution on A-site ions from $LaMnO_3$ perovskites by acid etching was investigated [9]. The outcome of acid etching is the incremental amount and the mobility of surface oxygen species, ulteriorly improving the catalytic effect. Co-terminated surface of $Sr_{0.6}La_{0.4}CoO_{3-\delta}$ was exposed by etching the inactive Sr/La–O termination. The localized unsaturated coordination microenvironment promoted the activation of surface oxygen site, enhancing the surface reactivity [11]. These conclusions uniformly highlighted the important role of acid etching on surface oxygen vacancies, but the change of intrinsic electronic structure remains an open question.

Oxygen vacancies undoubtedly display a pivotal role in superior catalytic performance, involving gaseous O_2 adsorption and activation, oxygen species migration and backfill, and participation in redox cycle reactions [2,12]. Notably, previous studies have brought much attention to the role of oxygen vacancy, but have ignored the correlations between surface properties and bulk electronic structure for a long time. The degree of vacancy formation not only reflects the oxygen-related character but also reveals the co-

* Corresponding author.
E-mail address: wqb@cumtb.edu.cn (Q. Wang).

https://doi.org/10.1016/j.cclet.2024.110260
1001-8417/

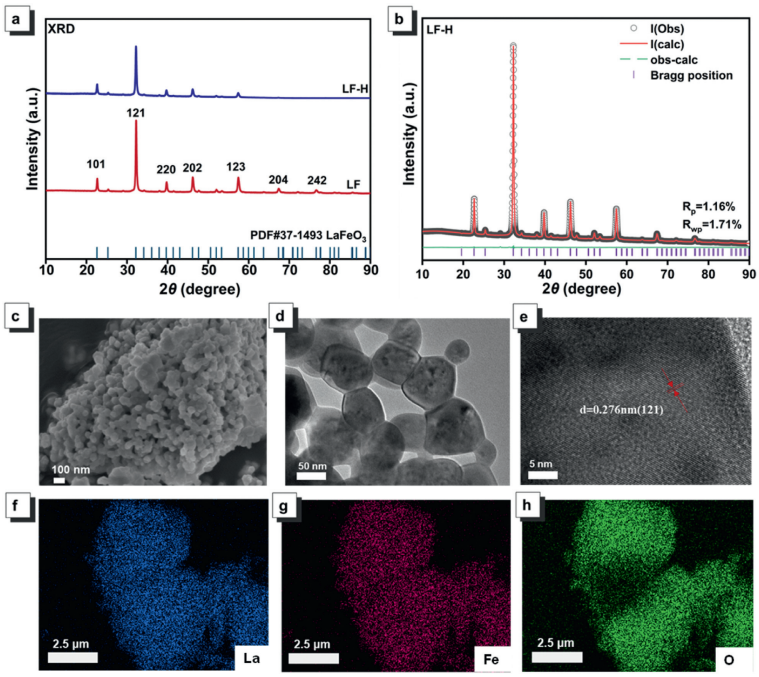

Fig. 1. (a) XRD patterns. (b) Rietveld refinements for LF-H. (c) SEM images for LF-H. (d, e) TEM images for LF-H and corresponding. (f-h) La, Fe, O EDS mappings for LF-H.

valent interaction between TM 3d and O 2p in the perovskite crystals. The transition metal oxidations with more covalency usually exhibit higher oxygen vacancy concentrations. Hwang proved the positive correlation between covalency and oxygen vacancy formation in conjunction with theoretical calculations and experiments [13]. Hence, the requisite of revisiting and investigating the role of acid etching has ensured to study inherent electronic nature and enhanced the catalytic activity at the atomic level.

Herein, we employed a wet-etching method to modulate the $LaFeO_3$ perovskite (LF) surface. A small concertation of La deficiency can boost the catalytic activity toward CO oxidation, and toluene oxidation. Surface treatment can alter octahedral distortion to abbreviate Fe–O bond length, inducing the formation of Fe^{4+} species. The introduction of oxygen vacancies facilitates surface activity and bulk phase mobility of lattice oxygen, heightening the availability of lattice oxygen. Furthermore, the interaction between metal and oxygen is investigated by theoretical calculation and O K-edge. The higher covalency for the $LaFeO_3$ with acid etching (LF-H) could reduce the energic barrier of the formation of oxygen vacancies and oxygen migration barrier, ulteriorly improving the catalytic properties. The enhanced activities for the perovskite-type materials could be rationalized by the enhanced Fe 3d and O 2p covalency. An in-depth understanding of the changes in the electronic structure plays a vital role in establishing unambiguous structure-property relationships in pursuit of enhancive catalytic efficacy.

The LF catalysts were synthesized *via* the traditional sol-gel method. Subsequently, a certain amount of LF catalysts was thrown into the 0.2 mol/L dilute nitric acid for 1 h. The materials *via* acid etching were repeatedly washed with deionized water and ethanol. Ultimately, the samples were annealed in the muffle furnace at 200 °C for 2 h. The powders were labeled as LF-H. More details about characterization and density functional theory (DFT) calculations are attached to Supporting information.

X-ray diffraction (XRD) patterns were recorded to explore the crystal structure. Fig. 1a displays the XRD patterns of perfect $LaFeO_3$ and $LaFeO_3$ with the A-site deficiency *via* acid etching. As expected, the catalysts exhibit a typical perovskite phase and could be described with all the peaks indexed to $LaFeO_3$ structures in the Pbnm space group symmetry (JCPDS Card No. 74–2203). There are no additional crystal phases of La_2O_3 or FeO_x after acid surface treatment. Acid etching resulted in a decrease in the intensity of the diffraction peaks, indicating lattice contraction. Rietveld refinements were carried out with XRD patterns to further unveil the detailed structural information. The low reliable factors (R_{wp} and R_p) suggest a good fitting between observed and calculated profiles (Fig. 1b and Fig. S1 in Supporting information, and Table 1). La occupy refined result of LF is 0.992, corresponding to the theoretical stoichiometric ratio roughly. After acid treatment, a small concentration of La is leached, and the La/Fe ratio (0.974) is slightly lower than the ratio of LF, which is in good agreement with ICP data (Table S2 in Supporting information). Acid etching led to a reduction in the average Fe-O bond length from 2.0098 Å to 2.0091 Å (Table S3 in Supporting information). The deformation degree δ of FeO_6 octahedron from the ideal symmetric structure is evaluated by the variance of Fe-O bond length. The increased deformation degree also indicated etching resulted in lattice distortion. As shown in Fig. 1c, the overall surface morphologies of as-synthesized catalysts were observed by scanning electron microscopy (SEM). The samples contain highly agglomerated nano-sized sphere particles. The size of LF-H perovskite is located in the range of 20–100 nm, which is similar to the BET surface areas (Fig. 1d and Fig. S4 in Supporting information). The inter-planar diffraction plane for both catalysts could also be performed by HRTEM (Fig. 1e). HRTEM images recorded in Fig. S3 (Supporting information) revealed that the interplanar spacing was 0.277 nm and 0.276 nm for LF and LF-H catalysts, respectively. Lattice space contraction implied structure distortion. The lattice fringe distances of 0.276 nm for LF-H perovskites match well with the (121) reflections in the corresponding XRD data [14]. We observed a homogenous mapping of La, Fe, and O elements through EDS analysis (Figs. 1f-h). Overall, these findings verify the high purity and structural distortion, which provides a basis for an in-depth understanding of the effect of A deficiency on the electronic structure and oxygen-related properties.

A-site deficiency exerts a considerable effect on tuning the valence of B-site and the nature of oxygen ligands. A-site deficiency

Table 1
ICP data, La and O occupy from Rietveld refinements, XPS analysis data, CO and toluene oxidation activity of the samples.

Catalysts	ICP/(molar ratio)	Rietveld refinements		XPS[a]		H_2-TPR[b]	CO oxidation/°C		Toluene oxidation/°C	
	La/Fe	La occupy	O occupy	Fe^{3+}/Fe^{4+}	O_{ads}/O_{latt}	H_2 Consumption (mmol g^{-1})	T_{50}	T_{90}	T_{50}	T_{90}
LF	0.992	0.992	1	2.09	1.80	0.831	330	369	293	328
LF-H	0.971	0.974	0.992	1.95	1.85	0.974	270	311	262	283

[a] Calculated by fitting XPS data.
[b] Obtained by peak area calculation using CuO as a reference.

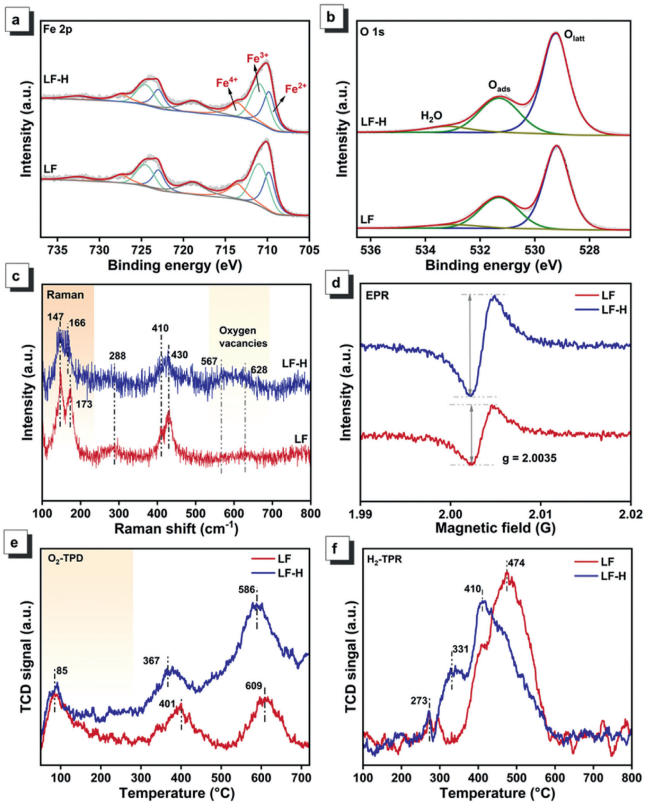

Fig. 2. (a) XPS spectrum of Fe 2p. (b) O 1s spectra. (c) Raman spectrum. (d) EPR. (e) O_2-TPD pattern. (f) H_2-TPR pattern.

in the $A_xB_yO_z$ perovskite systems could give rise to an imbalance in net charge. The missing positive charge can be compensated directly by B-site TM cations and oxygen vacancies to balance the overall charge neutrality. Electronic regulation causes valence increment of TM cations and the introduction of ligand holes. To elucidate the possible electronic structure change, X-ray photoelectron spectroscopy (XPS) as a surface-sensitive technique was implemented. XPS analysis containing La 3d, Fe 2p, and O 1s were explored in detail, as displayed in Figs. 2a and b and Fig. S6 (Supporting information). For the Fe XPS spectrum, a double-peaked spectrum and two shake-up satellite peaks are observed, manifesting the existence of a multi-component of Fe ions with different formal valence states [15]. The double-peaked spectrogram is assigned to Fe $2p_{3/2}$ (~710.2 eV) and Fe $2p_{1/2}$ (~724 eV). These spectra have been deconvoluted into three peaks, including Fe^{2+} (~709.8 eV), Fe^{3+} (~711 eV), and Fe^{4+} (~713.7 eV) species, respectively. The detailed analysis results attained from the XPS spectrum are summarized in Table S4 (Supporting information). LF-H catalysts have a lower Fe^{3+}/Fe^{4+} ratio (1.95) compared to LF (2.09) (Table 1). The average mixed-valence resting state of Fe states for LF (~2.90) and LF-H (~2.99) is examined. Specifically, a slight increase in Fe valence can be observed after acid etching. Enhancing Fe cation oxidation states can be considered to lessen the number of d electrons and increase the metal ion electronegativity owing to decreased electron shielding. A certain amount of Fe^{4+} species with an optimal e_g orbital filling ($t_{2g}^3e_g^1$) exist in the LF-H perovskites. A higher oxidation state of Fe cation is normally associated with elevated oxygen activity [16,17]. Mefford group reported that the d bands of Cobalt have greater overlapping with the s, p orbitals of oxygen due to the increase of the Co oxidation state, which leads to enhanced lattice oxygen activity [18]. The oxygen characteristics modulated by acid etching could also be analyzed by the O 1s spectrum. The O 1s spectra were deconvoluted into three peaks, including lattice oxygen (O_{latt} ~529.2 eV), surface adsorbed oxygen (O_{ads} ~531.3 eV), and adsorbed molecular water H_2O (~533.2 eV). The relative O_{latt} contention was qualified by integrating the peak area. After acid etching, the ratio of O_{latt}/O_{ads} increased from 1.81 to 1.84, tabulated in Table 1. In the typical MVK mechanism, surface lattice oxygen species could participate in heterogeneous catalysis. The molecular O_2 can be adsorped and activated over oxygen vacancies, and then activated oxygen can be readily transferred to replenish surface lattice oxygen consumed.

Raman spectroscopy was adopted to examine the vibration modes that correlate with oxygen vacancies in Fig. 2c. For pure $LaFeO_3$, the peaks observed in 147 and 173 cm^{-1} are assigned to an A_g mode associated with the vibration of La cations [19]. The scattering in 288 cm^{-1} is attributed to the FeO_6 octahedra tilt (T) modes. The band detected in 430 cm^{-1} is ascribed to oxygen octahedral bending vibrations (B) [20]. The Raman mode around 628 cm^{-1} corresponded to oxygen stretching vibrations (S) in conjunction with broaden overlapping contributions from longitudinal optic (LO) phonon modes [21,22]. There is a loss of low-frequency A-mode vibrations below 200 cm^{-1}, which can be primarily in concordance with the A-site deficiency. The lower wavenumber offset and decreased intensity further confirm the A-site deficiency. The attenuated La-O interaction could potentially activate the lattice oxygen. Besides, a series of modes located in the range of 600–700 cm^{-1} have been verified to be in good agreement with oxygen vacancies presentation [23]. The presence of these vacancies is further confirmed by electron paramagnetic resonance (EPR) in Fig. 2d. The higher resonance peak of oxygen vacancies at the location of $g = 2.003$ for LF-H perovskites with unpaired electrons trapped was detected compared to LF samples, which provides direct evidence of richer oxygen vacancies.

The capability to activate oxygen exerts a considerable influence on the catalytic performance of perovskites in heterogeneous catalytic reactions [24]. The results of O_2 temperature-programmed desorption (O_2-TPD) are shown in Fig. 2e. There are three oxygen desorption peaks in the temperature range of 100~700 °C. The peak α at ~85 °C is assigned to physical adsorption oxygen species desorption, while the peak β at about ~367 °C is attributed to chemisorbed surface-active oxygen species (O^{2-}, O^-). The peak γ at ~586 °C for LF-H is corresponding to the surface lattice oxygen (O^{2-}). As displayed, the oxygen desorption peaks shifted to a lower temperature after acid etching, suggesting acid etching could accelerate active oxygen migration from the subsurface to the sur-

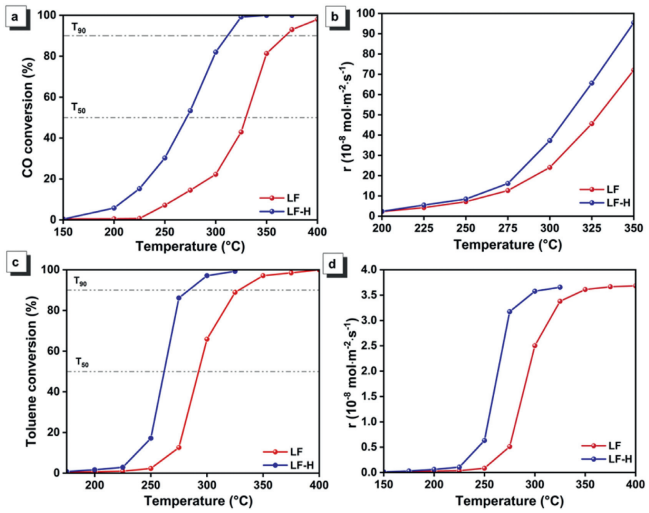

Fig. 3. Catalytic oxidation performance. (a) CO catalytic activity. (b) Surface area normalized reaction rate of CO oxidation. (c) Toluene catalytic activity. (d) Surface area normalized reaction rate of Toluene oxidation.

face [25]. The increased surface oxygen vacancies after acid etching promote the adsorption of oxygen species. H_2-TPR was employed to analyze the chemical adsorption capacity and redox behavior of the catalysts. The H_2-TPR profiles for LF and LF-H are displayed in Fig. 2f. These two catalysts are uncovered to undergo three main reduction processes. The related reduction processes for LF-H are listed as follows: (a) the reduction of a small amount of reactive surface oxygen species at 273 °C, (b) the reduction of Fe^{4+} to Fe^{3+} at approximately 331 °C, (c) the reduction of Fe^{3+} to Fe^{2+} at approximately 410 °C. The lower reduction temperature for LF-H exhibits excellent redox activity. The peaks shift to the lower temperature reveals more active sites are exposed on the catalyst surface due to the removal of La–O caused by etching. The higher total H_2 consumption (0.974 mmol/g) of LF-H gives compelling evidence on the better redox capability compared to LF (0.831 mmol/g).

To further exploit the potential effect of A-site cation deficiency, we then evaluated the effect of acid etching on catalytic performance. The LF-H catalysts exhibit apparently enhanced catalytic activity in comparison with faultless $LaFeO_3$ for both CO and toluene oxidation (Figs. 3a and b and Table 1). For CO catalytic oxidation, the T50 values of LF and LF-H are 330 °C and 270 °C, and the T90 values of LF and LF-H are 369 °C and 311 °C, respectively. For Toluene catalytic combustion, the T50 and T90 values for LF are 293 °C and 328 °C, and those for LF–H are 262 °C and 283 °C, respectively. The T_{90} values of toluene and CO oxidation for LF–H are 45 °C and 58 °C lower than those for LF, respectively. Additionally, the surface area normalized reaction rates were recorded to assess the catalytic performance (Figs. 3c and d). The surface area normalized reaction rate of LF-H is much higher than that of LF samples. For instance, the toluene oxidation rate of LF-H (36.27×10^{-8} mol m^{-2} s^{-1}) is 2.51 times than that of LF (14.45×10^{-8} mol m^{-2} s^{-1}) at 300°C. Therefore, the higher catalytic activity has been achieved *via* acid etching. In other words, acid etching as an effective strategy could enhance catalytic activity, but the necessity of understanding the underlying mechanism still remains.

The change in the perovskite surface composition induced by etching could give rise to a change in the electronic structure, especially the interaction between metal and oxygen. There are three features labeled A, B, and C (Fig. 4a). Feature A is attributed to the unoccupied 3d t_{2g} states with minor hybridization with O 2p character. Feature B is assigned to O 2p nonbonding derived states, with only a small covalency with Fe 3d, while Feature C is associated with Fe 3d–O 2p bonding states [26]. The valence (CBM) descends from 0.761 eV to 0.537 eV. The UV–vis spectrum in Fig. 4b also exhibits adsorption features in the energy interval. An adsorption area at 200–300 nm is attributed to the ligand-to-metal charge transfer (LMCT), while the broad absorption features at 550–700 nm originate from d-d electronic excitations on Fe cations due to the existence of occupied d-orbitals on Fe ions [27]. The intensity in the adsorption range of 200–300 nm in LF-H is significantly reduced, indicating the lower charge transfer energy and larger covalency. High covalency results in a certain loss of ionic charge, which is in accordance with the XPS data. The inset indicates that LF-H catalysts have a lower shift in the adsorption edge than LF. Band gap in LF-H (2.13 eV) is slightly narrower relative to that in LF (2.16 eV), which manifests the electrons are feasible to get activated and transferred after acid etching [28].

The O K-edge XAS spectra were further employed to evaluate the entire electronic structure of the perovskites. Fig. 4c exhibits the normalized O K-edge XAS spectrum of the LF and LF-H catalysts. The characteristic peaks located at ~529.6 eV and ~531 eV attributed to the motivation from O 1s to the unoccupied hybridized O 2p–Fe 3d sates, including the hybridization of O 2p and the Fe 3d e_g states (σ symmetry) and the covalency with the Fe 3d t_{2g} states (π symmetry) owing to the dipole rules. The regions II between ~532 eV and ~538 eV corresponds to the mixing of O 2p and La 5d states. Region III is assigned to the transition from O 1s to O 2p–La 5d and O 2p–Fe 4sp. The higher pre-peak intensity and peak width of LF-H increase, uncovering an increase in Fe 3d–O 2p covalency after acid etching. The increase of Fe valence state after acid etching is consistent with higher metal-oxygen covalency. Besides, a reduction of the hybridization between O 2p and La 5d could be regarded as a side-effect of the enhancement of Fe 3d–O 2p covalency. The decrease in La–O interaction may be also related to the augmentable oxygen activity.

We further verified the impact of acid etching on the above-obtained Fe–O band properties by calculating the crystal orbital Hamilton population (COHP). The metal-oxygen covalency was evaluated by the integral of -COHP value and the corresponding value is −0.863 for LF-H and −0.823 for LF, respectively. The larger absolute value of ICOHP gives convincing evidence of Fe–O covalency. To shed light on the change in electronic structure, PDOS was calculated in Fig. 4d. PDOS produces a gap in the resulting band structure with a Fe 3d e_g band above the valence band edge. The band gap of LF-H catalysts is reduced. The Fe 3d/O 2p π^* bands cross the Fermi level, accompanied by the oxygen holes. Hole doping of the O 2p band could result in effective electronic screening effects, thereby getting a lower electron transfer barrier [29]. The unoccupied states include the Fe 3d e_g hole states (inside the dotted box in Fig. 4e) arising from the localized oxidation of Fe^{3+} ions to form Fe^{4+}. The increase in the formal Fe oxidation state drives the formation of oxygen holes on the oxygen ligands, contributing to the generation of oxygen vacancies [30]. Figs. 4f and g display the average onsite energies of the Fe 3d and O 2p bands relative to the Fermi level. The charge transfer energy can be defined as the relative energy value of Fe 3d and O 2p. The energy difference of LF-H is 3.09 eV, while that of LF is 3.27 eV. The charge transfer energy is proportional to the extent of metal 3d and oxygen 2p covalency. High covalency in the perovskite oxide manifests the ability of the TM active site to form more distinct covalent interactions with frontier molecular orbitals (HOMO and LUMO) of surface reactant species *via* a larger overlap integral and thus facilitates electron transfer in redox reactions [31].

Besides, the enhanced metal-oxygen bonding can facilitate electron-hopping in the Fe^{3+}–O–Fe^{4+} backbone (Fig. 4h) [32]. Due to the strong overlapping between Fe 3d orbital and O 2p orbital resulting from the unique structure arrangement, the elec-

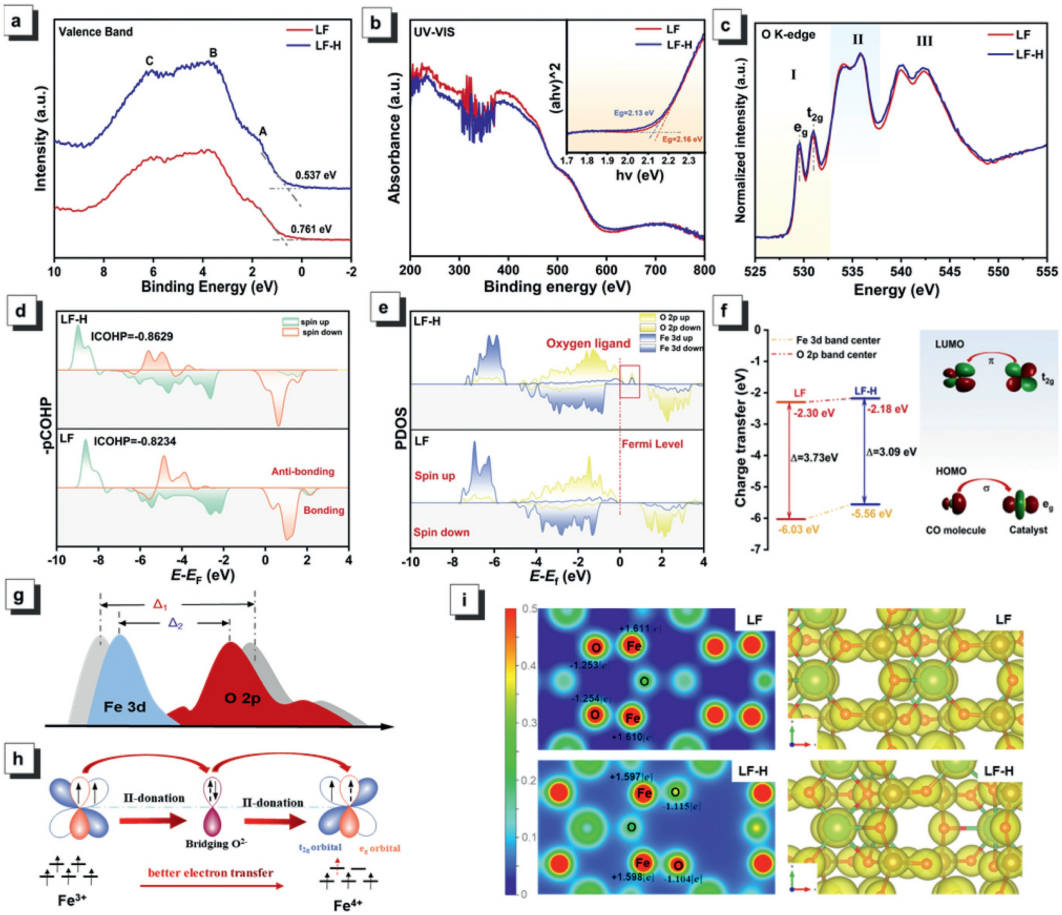

Fig. 4. (a) Valence band spectrum. (b) UV–vis absorption spectra. (c) The O K-edge XAS spectra. (d) Crystal orbital Hamilton populations (COHP) of the Fe–O bond. (e) The computed PDOS of Fe 3d and O 2p in (121) surface. (f) The charge transfer energy (left) and the interaction between reactant molecule (CO as an example) with the transition metal oxidations (right). (g) Schematic diagram of the Fe 3d (blue) and O 2p (red) band relative positions. (h) Schematic illustration of intramolecular electron transfer. (i) Bader charge variation of Fe and O (left) and charge density plots with a top view of LF and LF-H samples (right).

tronic transport is realized by the TM–O–TM bond, namely the Zerner double exchange regime. The electron transport depends on the TM–O–TM network and valence alternation of TMs, promoting the generation of Fe^{4+}/Fe^{3+} redox cycle. Shao-Horn groups reckon the active redox couple of B-site has a larger O 2p character above the Fermi Level in high TM–O covalency perovskite oxides, promoting the charge transfer [33]. The unique structure arrangement could contribute to the lattice O^{2-} migration to surface. TM–O covalency can increase the capabilities of charge transfer and the higher chemical states. Interestingly, the enhanced Fe–O covalency and low oxygen vacancy formation energies may seem contradictory, which is likely to be attributed to weakened La–O interaction.

Charge distribution can give a more accurate determination of the TM–O covalent characteristic. As such, we further investigated the electron delocalization by computing effective Bader charges before and after acid etching (Fig. 4i). It is overestimated that the oxidation state of the cation has a decisive effect on the electronic structure. Bader charge analysis is an effective instrument to help quantify the ionicity *vs.* covalency of TM–O. In general, the more the Bader charge deviates from the formal oxidation state, the stronger covalency is in the bond [34]. As calculated, the Bader charge in LF is +1.611 for Fe and −1.253 for O, respectively. The Fe and O ions in LF-H have Bader charges of +1.597 and −1.115, which deviate from their ionic charge of +3 (Fe cations) and −2 (O ions). The greater charge deviation reflects the strong Fe–O covalent character. Therefore, the Fe–O bonding in LF-H is slightly more covalent than that in LF. The partial covalency of Fe–O bonding realizes electronic sharing between the lattice O^{2-} cations with the Fe ions.

It has been recognized that larger covalency could reduce the oxygen vacancy formation energy, resulting in incremental favorability for oxygen transport. The effect of etching on oxygen vacancy formation energy was studied. As expected, the oxygen vacancy formation energy of LF-H decreased, which is consistent with the experiment results. Acid etching could create oxygen hole states, which promotes compensating electrons released upon the oxygen vacancies formation, thereby decreasing the vacancies formation energy barrier. In addition, the surface lattice oxygen diffusions on the catalyst surface and subsurface mostly rely on the oxygen vacancy. The oxygen cations at the lattice point hop into the vacancy position (Fig. 5). In a word, oxygen migrations in perovskite-type oxidations occur *via* the vacancy mechanism, in which oxygen diffusion is facilitated through surface oxygen jumping from occupied oxygen positions to neighboring vacancy positions [35]. Therefore, defected $LaFeO_3$ perovskites with an oxygen vacancy on the surface and in the subsurface are constructed. The energy barriers of oxygen diffusion from the subsurface layer to the surface layer for LF and LF-H are explored. The calculated results are 0.544 eV for LF and 0.507 eV for LF-H, respectively. As it turns out, the LF-H with larger covalence could lessen the energy of oxygen vacancy formation and enhance oxygen kinetics. These results highlight the benefit of acid etching as an effective tactic to boost the mobility of oxygen in perovskite oxides.

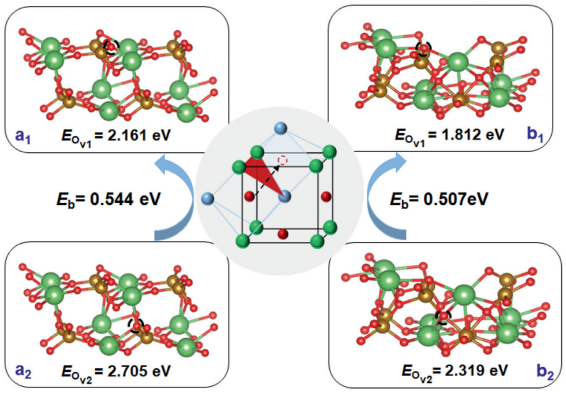

Fig. 5. The oxygen vacancy formation energy (E_{ov}) and oxygen diffusion energy barrier (E_b) over the (a_1, a_2) LF substrate; (b_1, b_2) LF-H substrate; E_{ov1} and E_{ov2} represent the surface and subsurface oxygen vacancy formation energy, respectively. The O cation marked with the black dotted circle manifests that it has been dislodged.

In situ DRIFTS was employed to further discern intermediate species generated in the reaction process and reveal the roles of acid etching. Profiles in Fig. 6 and Fig. S7 (Supporting information) illustrate the time-clocked toluene adsorption states on the LF and LF-H catalysts at 30 °C. At first glance, strong –OH peaks at 3200–3500 cm^{-1} appeared, indicating a methyl dehydrogenation during toluene adsorption. The peaks at 1591 and 1496 cm^{-1} were indicative of aromatic ring out-of-plane and in-plane vibrations [36–38]. Especially, the peak around 1680 cm^{-1} (=C=O) represented the signal of benzoquinone [39]. The peaks at 1272 and 1653 cm^{-1} corresponded to the C–O vibration peak of benzaldehyde, and the peaks located at 1315, 1414, 1540, and 1565 cm^{-1} could be ascribed to the –COO– stretching vibrations of benzoate [40]. The peak at 1469 cm^{-1} was assigned to $-CH_2-$ of benzyl alcohol [41]. In addition, the three peaks at 1081, 1049, and 1029 cm^{-1} were related to the C–O stretching vibration of benzyl alcohol species ($pH-CH_2-O-$), while the peak at 1209 cm^{-1} was assigned to the phenolate species (=C–O–) [42]. The relevant details of the infrared peaks corresponding to the intermediates were tabulated in Table S5 (Supporting information). It was discernible to find that the strength of the adsorption peak and vibrational peaks of intermediates over LF-H catalysts exhibited significant growth. This was related to the fact that the antibonding states exhibit greater oxygen character due to the enhanced Fe 3d–O 2p covalency, enhancing adsorption capacity. On the other hand, the amount of –COO– species was the embodiment of methyl activation ability, which was the vital process of toluene oxidation [39]. The significant difference of –COO– species at 1315 cm^{-1} displays higher covalency of LF-H catalysts is more favorable for initial oxidation of toluene.

The temperature of the transient *in situ* DRIFTS experiment was carried out to further observe the variation of intermediates and elucidate the role of acid etching (Figs. 6c and d). The specific evolution curves of characteristic bands for LF-H were displayed between 260 °C and 300 °C in Fig. S8 (Supporting information). Toluene and primary oxidation products undergo further degradations, leading to dynamic accumulation and consumption of multiple intermediates. For LF catalysts, numerous unsaturated benzoates located at 1540 and 1393 cm^{-1} accumulated, and a weak band of maleic anhydride (1300 cm^{-1}) appeared, indicating only a tiny fraction of toluene was deeply oxidized. Despite the presence of the ring-contained intermediates, it was still difficult to be oxidized into byproducts (bicarbonate, carbonate, *etc.*) below the temperature of 300 °C. Apparently, more micromolecule chain saturated/unsaturated fatty acids were generated on the LF-H surface. The peak at 1179 and 1139 cm^{-1} were attributed to the C–O stretching vibration mode of benzyl alcohol. The benzyl alcohol species accumulated and the peak position red shifted to 1115 cm^{-1} as the temperature rose to 260 °C. The C=C stretching vibration of the aromatic ring (1591 cm^{-1}) disappeared over 260 °C. The accumulation of bicarbonate could be observed at 1622 cm^{-1}, which convincingly proved that toluene was ulteriorly oxidized to CO_2 and H_2O. The intensity of –COO– stretching vibrations of benzoate (1377 cm^{-1}) and the peak of –CHO benzaldehyde (1250 cm^{-1}) obviously dropped and the broaden stripe

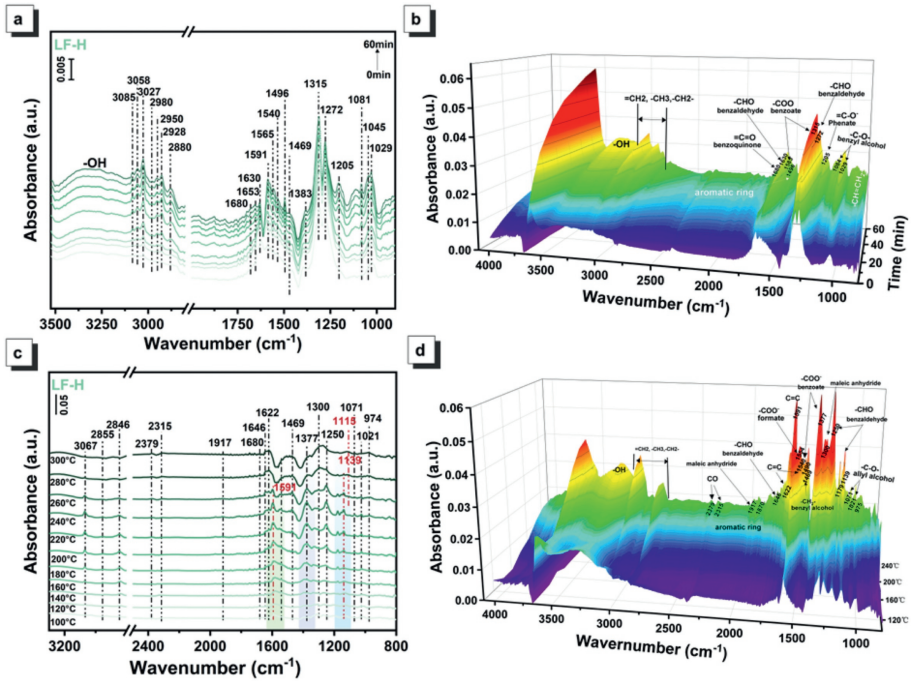

Fig. 6. (a, b) Time-resolved *in-situ* DRIFTS profiles of toluene adsorption at 30 °C. (c, d) Toluene oxidation under different reaction temperatures for LF-H catalysts. Reaction conditions: 100 mL/min, 300 ppm toluene with 21% O_2, 79% N_2 balance.

of maleic anhydride (1300 cm^{-1}) rose. In total, toluene and primary intermediates were continuously degraded, and abundant ring-opened products (maleic anhydride) took shape. The changes in infrared spectra coincided with the conversion of toluene at *ca.* 263 °C (T_{90}). Due to the conclusions above, toluene oxidation occurred as the following pathway: the benzyl–benzyl alcohol–benzaldehyde–benzoate–anhydride–CO_2 and H_2O. The results further explained that larger TM–O covalency induced by acid etching promoted the toluene oxidation process. The adsorption and oxidation of CO were investigated by *in situ* DRIFTS and the results are shown in Figs. S9 and S10 (Supporting information).

In conclusion, we have demonstrated that acid etching is an effective strategy to boost the catalyst activity. The method can produce oxygen vacancies and promote the elevated Fe oxidation states. The hybridization of the Fe–O bond has been found to increase after acid etching, which is measured by XAS O K-edge and DFT calculation. The unoccupied states of the O 2p band around the Fermi level exhibit the degree of oxygen vacancies in a highly Fe–O covalency system. Oxygen vacancy can allow for the rationalization of the enhanced catalyst activity in conjunction with the modulation of the Fermi energy through TM 3d and oxygen 2p covalency at the surface. Hence, the combination of surface chemistry and bulk electronic structure could be employed to guide the design of catalysts.

Declaration of competing interest

The authors declare that they have no known competing financial interests or personal relationships that could have appeared to influence the work reported in this paper.

Acknowledgments

The authors acknowledge the financial support provided by the National Natural Science Foundation of China (Nos. 22376178, 22322606, 22276105), the National Key Research and Development Program of China (No. 2022YFC3704300), and the Beijing Natural Science Foundation (No. 8222054).

Supplementary materials

Supplementary material associated with this article can be found, in the online version, at doi:10.1016/j.cclet.2024.110260.

References

[1] Y.J. Shen, J. Deng, L.P. Han, W. Ren, D.S. Zhang, Environ. Sci. Technol. 56 (2022) 10433–10441.
[2] Z.A. Su, W.H. Yang, C.Z. Wang, et al., Environ. Sci. Technol. 54 (2020) 12684–12692.
[3] X.X. Duan, T. Zhao, B. Niu, et al., Adv. Sci. 10 (2023) 2205054.
[4] Y. Yang, W.Z. Si, Y. Peng, et al., Appl. Catal. B: Environ. 340 (2024) 123142.
[5] Y.R. Fang, Q. Zhang, H. Zhang, et al., Angew. Chem. Int. Ed. 61 (2022) e202212273.
[6] X.M. Xu, Y.L. Pan, Y.J. Zhong, et al., Adv. Sci. 9 (2022) 2200530.
[7] D.J. Li, Y. Meng, Y.X. Zhang, et al., Adv. Funct. Mater. 33 (2023) 2302866.
[8] X.Y. Wang, X.B. Li, X.F. Chu, et al., Adv. Funct. Mater. 31 (2021) 2006439.
[9] W.Z. Si, Y. Wang, Y. Peng, J.H. Li, Angew. Chem. 127 (2015) 8065–8068.
[10] Q.L. Yang, J.Y. Li, D. Wang, Y. Peng, J.H. Li, Catal. Today 376 (2021) 205–210.
[11] X.B. Li, X.Y. Wang, J.F. Ding, et al., ACS Catal. 13 (2023) 6338–6350.
[12] Z.A. Su, W.Z. Si, H. Liu, et al., Environ. Sci. Technol. 55 (2021) 12630–12639.
[13] J. Hwang, R.R. Rao, L. Giordano, et al., Science 358 (2017) 751–756.
[14] K. Wang, C. Han, Z.P. Shao, et al., Adv. Funct. Mater. 31 (2021) 2102089.
[15] X. Tian, C.H. Zheng, H.B. Zhao, Appl. Catal. B: Environ. 303 (2022) 120894.
[16] Z.Y. He, J. Zhang, Z.H. Gong, et al., Nat. Commun. 13 (2022) 2191.
[17] Y.Z. Wu, Y.Y. Zhao, P.L. Zhai, et al., Adv. Mater. 34 (2022) 2202523.
[18] J.T. Mefford, X. Rong, A.M. Abakumov, et al., Nat. Commun. 7 (2016) 11053.
[19] C.N. Zhao, X.L. Zhang, M. Yu, et al., Adv. Mater. 32 (2020) 2006145.
[20] B.P. Barbero, J.A. Gamboa, L.E. Cadús, Appl. Catal. B: Environ. 65 (2006) 21–30.
[21] W.J. Sun, H.Z. Wei, L.Y. An, et al., Appl. Catal. B: Environ. 245 (2019) 20–28.
[22] M.C. Weber, M. Guennou, H.J. Zhao, et al., Phys. Rev. B 94 (2016) 214103.
[23] P. Eyméoud, C. Turquat, C. Pardanaud, C. Leroux, A. Merlen, Mater. Lett. 330 (2023) 133296.
[24] Y.C. Wei, J. Liu, Z. Zhao, et al., Angew. Chem. 123 (2011) 2374–2377.
[25] Q. Yu, C.T. Li, J.G. Zhao, et al., Appl. Catal. B: Environ. 327 (2023) 122441.
[26] H. Liu, S. Yang, G.M. Wang, et al., Environ. Sci. Technol. 56 (2022) 16325–16335.
[27] A. Bean" Getsoian, Z. Zhai, A.T. Bell, J. Am. Chem. Soc. 136 (2014) 13684–13697.
[28] H. Chang, E. Bjørgum, O. Mihai, et al., ACS Catal. 10 (2020) 3707–3719.
[29] Y.M. Sun, H.B. Liao, J.R. Wang, et al., Nat. Catal. 3 (2020) 554–563.
[30] Z.F. Huang, S.B. Xi, J.J. Song, et al., Nat. Commun. 12 (2021) 3992.
[31] J. Simböck, M. Ghiasi, S. Schönebaum, et al., Nat. Commun. 11 (2020) 652.
[32] N. Zhang, C. Wang, J. Chen, Y. Chai, EcoMat 5 (2023) e12290.
[33] J. Suntivich, K.J. May, H.A. Gasteiger, J.B. Goodenough, Y. Shao-Horn, Science 334 (2011) 1383–1385.
[34] A.B. Muñoz-García, D.E. Bugaris, M. Pavone, et al., J. Am. Chem. Soc. 134 (2012) 6826–6833.
[35] J.J. Mao, J. Iocozzia, J.Y. Huang, et al., Energy Environ. Sci. 11 (2018) 772–799.
[36] M.L. Xiao, D.W. Han, X.Q. Yang, et al., Appl. Catal. B: Environ. 323 (2023) 122173.
[37] Q.Y. Wang, Y.X. Li, A. Serrano-Lotina, et al., J. Am. Chem. Soc. 143 (2021) 196–205.
[38] Y.W. Ren, X. Lei, H. Wang, J.P. Xiao, Z.P. Qu, ACS Catal. 13 (2023) 8293–8306.
[39] W.H. Yang, Y. Wang, W.N. Yang, et al., Appl. Mater. Interfaces 13 (2021) 2753–2764.
[40] Y.J. Shen, J. Deng, X.N. Hu, et al., Environ. Sci. Technol. 57 (2023) 1797–1806.
[41] W.H. Yang, Z.A. Su, Z.H. Xu, et al., Appl. Catal. B: Environ. 260 (2020) 118150.
[42] H. Liu, J.J. Chen, Y. Wang, et al., Environ. Sci. Technol. 56 (2022) 4467–4476.